Heliyon 10 (2024) e39350

Contents lists available at ScienceDirect

Heliyon

journal homepage: www.cell.com/heliyon

Research article

Interfacial insights: [6]-Gingerol monolayers at the air-water interface and beyond

Lara Adwan [a,b], Laura Dotor [a,b,c], María Graciela Pino [a,b,c], Adriana Gil [a,b], Santiago Martin [a,b,c], Pilar Cea [a,b,c,*]

[a] Departamento de Química Física, Facultad de Ciencias, Universidad de Zaragoza, 50009, Zaragoza, Spain
[b] Instituto de Nanociencia y Materiales de Aragón (INMA), CSIC-Universidad de Zaragoza, 50009, Zaragoza, Spain
[c] Laboratorio de Microscopias Avanzadas (LMA), Universidad de Zaragoza, 50018, Zaragoza, Spain

ARTICLE INFO

Keywords:
[6]-Gingerol
Langmuir films
Langmuir-Blodgett films
Surface behavior

ABSTRACT

Ginger is a culinary spice with a millennia-old tradition due to its extensive therapeutic applications, recently validated by scientific studies. In particular [6]-Gingerol, a key active molecule in ginger, exhibits extraordinary capabilities in addressing a wide spectrum of health issues. However, its therapeutic potential is limited by its rather low bioavailability. The incorporation of [6]-Gingerol into membrane systems of liposomes, micelles, or exosomes is a promising strategy to overcome this limitation. In this contribution, we report the hitherto unexplored surface properties of [6]-Gingerol at the air-water interface. Our comprehensive study, which includes a detailed analysis of surface pressure and surface potential vs. area per molecule isotherms, surface compression modulus, and Brewster Angle Microscopy, demonstrates the capability of [6]-Gingerol to form Langmuir films. These films can be transferred onto solid substrates, forming remarkably homogeneous Langmuir-Blodgett films which have been characterized by Quartz Crystal Microbalance and Atomic Force Microscopy. This study may be of interest as it paves the way for future research on introducing [6]-Gingerol into membrane systems and transporting it into living cells.

1. Introduction

Over the years, there has been a thorough examination of natural products in the search for bioactive compounds crucial for the development of novel drugs and therapies. The development of pharmacognosy in the early 20th century emphasized the botanical branch, while the expansion of synthetic chemistry in the 1990s broadened conventional approaches through high-throughput screening (HTS) of synthetic libraries [1]. Over the past two decades, there has been a renewed interest from both the scientific community and the general public in natural dietary agents found in fruits, vegetables, and spices, with ginger being one of the most widely studied. Ginger (*Zingiber officinale Roscoe*) is a plant from the Zingiberaceae family whose root has been used as a culinary spice and traditional medicine in Asia for over 5000 years [2]· Fresh ginger enhances the flavor of dishes, beverages, pickles, and even candy, adding fresh and mild pungent notes to the preparation. Moreover, ginger has a longstanding tradition as a medicine for addressing a variety of conditions including arthritis, rheumatism, muscular discomfort, atherosclerosis, cardiac palpitation, hypertension, migraine, ulcers, nausea, indigestion, asthma, depression, impotence, painful menstrual periods, cold and flu-like symptoms, among

* Corresponding author. Departamento de Química Física, Facultad de Ciencias, Universidad de Zaragoza, 50009, Zaragoza, Spain.
E-mail address: pilarcea@unizar.es (P. Cea).

https://doi.org/10.1016/j.heliyon.2024.e39350
Received 18 July 2024; Received in revised form 12 September 2024; Accepted 11 October 2024
Available online 15 October 2024

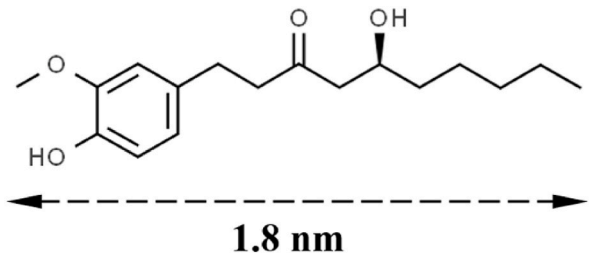

Fig. 1. Chemical structure of [6]-Gingerol: ((5S)-5-hydroxy-1-(4-hydroxy-3-methoxyphenyl)decan-3-one).

others. In addition to millennia of traditional use, numerous clinical studies evidence the efficacy of ginger in addressing gastric dysfunctions [3], vascular diseases [4,5], ischemic stroke [6], metabolic syndrome [7,8], diabetes [9,10], bone and joint disorders [11], emesis [12], anti-obesity effects [13,14], anti-infection effects (e.g., suppression of *Helicobacter pylori*) [15], age-related neurological disorders [16,17], and cancer (including tumor suppression, enhancement in the efficacy of chemotherapeutic drugs, and reduction of the side effects of chemo- and radiotherapy) [18,19]. Comparative studies of cancer incidence, particularly gastrointestinal, prostate, and breast cancers, show significantly lower rates in Southeast Asian countries compared to Western countries (Europe and the USA) [20,21]. It is believed that phenolic compounds present in this family of species, such as ginger and turmeric, may contribute to suppressing the transformative, hyper-proliferative, and inflammatory processes underlying carcinogenesis, angiogenesis, and metastasis. Ginger is generally recognized as safe (GRAS) by the USA Food and Drug Administration, FDA, when used in typical food quantities, but large doses carry the potential for adverse reactions (heartburn, diarrhea, mouth irritation, arrhythmia, and immunoglobulin E (IgE) allergic reaction). However, this USA agency has not recognized yet the use of ginger as a drug. The EMA (European Medicines Agency) accepts the well-established and traditional use of ginger in the prevention of nausea and vomiting caused by motion sickness, as well as the traditional employment of ginger in the symptomatic treatment of mild spasmodic disorders of the gastrointestinal tract, which includes abdominal distension and flatulence.

At least 14 bioactive compounds have been identified in ginger, including phenolic compounds and terpenes [2]. Among these phytochemicals, gingerols are more prevalent (≈25 %) [22] than shogaols and paradols. [6]-Gingerol stands out as the most abundant of gingerols, while [4]-, [8]-, [10]-, and [12]-Gingerol are present in lower amounts [23]. [6]-Gingerol is partially responsible for the pungent flavor and the biological activity of fresh ginger. It is found in much higher amounts in fresh ginger roots compared to dried roots because drying results in dehydration and conversion into [6]-Shogaol. Chemically [6]-Gingerol is a beta-hydroxy ketone featuring a vanillyl group, as illustrated in Fig. 1. It has a length of approximately 1.8 nm in a fully extended disposition and a neutral charge, containing two hydrogen bond donor atoms and four hydrogen bond acceptor atoms, which enables intermolecular interactions. The high number of rotatable bonds (ten bonds) provides the molecule with a high conformational flexibility. It is rather insoluble in water, but it readily dissolves in organic solvents.

[6]-Gingerol is a relevant pharmacological component due to its reported anti-inflammatory, antioxidant, antiemetic, analgesic, antipyretic, anxiolytic, anti-infection, antihepatotoxic, and antitumoral properties [2,24–31]. Its potential as a cost-effective dietary agent for treating a wide variety of diseases warrants deep investigations to incorporate this compound in commercial applications across various sectors such as food, agronomic, and pharmaceutic industries. Nevertheless, its low water solubility results in limited oral absorption, rapid metabolism, and low bioavailability, which hampers its clinical applications [32,33]. To circumvent these issues, attention has been paid to the encapsulation of [6]-Gingerol through various nano-formulations [23], including vesicles [34], liposomes [35], and plant-derived exosome-like nanoparticles [36]. Furthermore, studying the affinity of [6]-Gingerol with the components of membrane systems and elucidating factors that may influence its entrapment efficiency, could aid in the design and optimization of drug delivery systems.

While the Langmuir technique is a well-known method for modelling cell membranes and their interactions with xenobiotics, drugs, nanoparticles, etc. [37,38] to the best of our knowledge, no studies on the surface behavior of [6]-Gingerol at the air-water interface have been reported. These studies at the air-water interface may help to determine the optimal composition in liposomal formulations incorporating such active components [39]. Given the potential of [6]-Gingerol in health applications and the fundamental interest in understanding its miscibility with membrane systems, mimicked through Langmuir and Langmuir-Blodgett methodologies, the aim of this contribution is to analyze the surface behavior of [6]-Gingerol at the air-water interface and the feasibility of transferring it onto solid supports. This will lay the groundwork for subsequent, more complex studies of this compound and its interaction with membrane components.

2. Materials and methods

2.1. Materials

10 mg of [6]-Gingerol (GIN, ≥98 %, Sigma-Aldrich) were dissolved in chloroform to prepare a stock solution of $6.9{\cdot}10^{-4}$ M. The stock solution underwent ultrasonic processing for 5 min to prepare diluted [6]-Gingerol solutions. All solutions were stored in a freezer to avoid degradation. Before their use, all solutions underwent ultrasonic processing for 3 min to prevent the formation of three-dimensional aggregates. Chloroform was purchased from Macron Fine Chemicals (≥99.8 %, CAS 67-66-3).

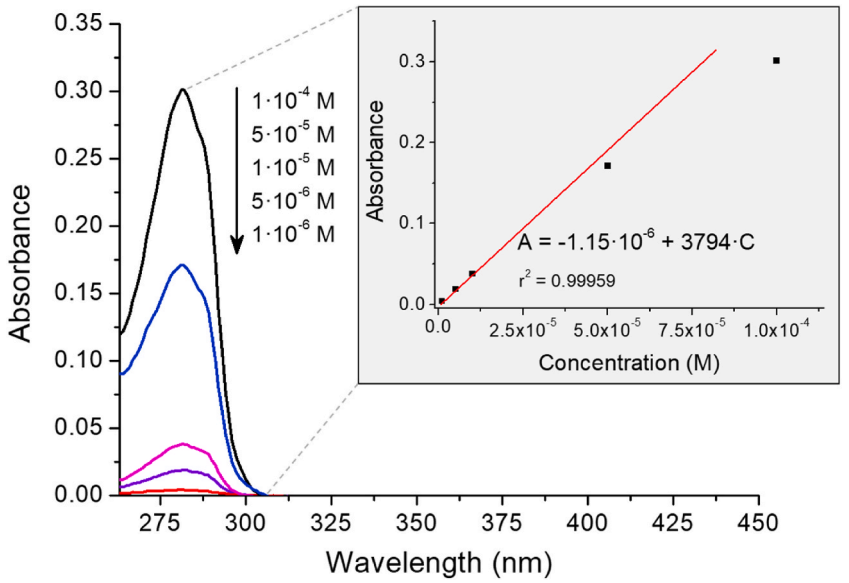

Fig. 2. UV–vis spectra of [6]-Gingerol in $CHCl_3$ at the indicated concentrations. Inset: absorbance vs. concentration at the maximum wavelength (282 nm).

2.2. Methods

UV–vis spectra. UV–vis spectra of [6]-Gingerol solutions were acquired on a Varian Cary 50 spectrophotometer using 1 cm quartz cuvettes. The background spectrum was recorded with a clean quartz cuvette filled with chloroform.

Surface pressure vs. area per molecule isotherms. Surface pressure vs. area per molecule (π-*A*) isotherms of [6]-Gingerol were recorded on a pure water subphase (Millipore Milli-Q purification system, resistivity 18.2 MΩ cm) using a KSV Nima KN 2003 Teflon trough (580 × 145 mm^2) following traditional methodologies in the area [40–43]. The surface pressure (π) was determined using a Wilhelmy paper plate pressure sensor. All the experimental setup was placed in a light-tight chamber that was in a semi-clean room with a constant temperature (21 ± 1 °C). The solution of [6]-Gingerol in chloroform was spread onto the water surface by using a 1 mL Hamilton syringe (Sigma Aldrich). A constant initial area per molecule of 2.15 $nm^2 \cdot molecule^{-1}$ was fixed. The solvent was allowed to evaporate for 15 min. During the compression of the monolayer, the trough barriers moved at a constant speed of 14.5 $cm^2\ min^{-1}$. To ensure reliability, all the π-A isotherms were recorded at least three times to confirm reproducibility.

Brewster Angle Microscopy (BAM). The formation of the [6]-Gingerol monolayer at the air-water interface was visualized using a mini-Brewster angle microscopy (mini-BAM) from Nanofilm Technologie GmbH. Simultaneously, the surface pressure-area per molecule (π-*A*) isotherm was recorded using a Nima Teflon trough (720 × 100 mm^2).

Surface potential vs. area per molecule isotherms. Surface pressure-area per molecule (π-*A*) and surface potential-area per molecule (ΔV-*A*) isotherms were registered simultaneously using a Nima Teflon trough (720 × 100 mm^2) and a Kelvin Probe provided by Nanofilm Technologie GmbH following previous methodologies in the area [44,45].

Langmuir-Blodgett (LB) films. Using the same experimental setup as before, selected films were transferred onto two types of substrates to form Langmuir-Blodgett (LB) films: mica and Quartz Crystal Microbalance (QCM) substrates. Muscovite mica sheets (Electron Microscopy Sciences, Cat. #71851–05, sheet size 25 × 75 mm, thickness 0.26–0.31 mm) were cut with a scissor to obtain 1 × 1 cm^2 mica substrates. Before use, mica substrates were exfoliated with adhesive tape to ensure a clean and homogeneous surface. The QCM substrate was a AT-cut quartz crystal patterned with circular gold electrodes on both sides. The QCM crystals used in this contribution had a diameter of 2.5 cm and a resonant frequency of 5 MHz. In all cases, the transference process was performed by a single withdrawal of the substrate initially immersed in the water subphase at a speed of 1 mm min^{-1}, i.e., the vertical dipping method (emersion) was used.

Atomic Force Microscopy (AFM). [6]-Gingerol LB films transferred on mica substrates were explored by AFM. The microscope was a Multimode 5 equipped with a Nanoscope V control unit from Bruker. Topographic images were obtained using RTESPA-150 tips (nominal frequency of 150 kHz, from Bruker) in air, employing Tapping mode at a scan rate of 1.0–1.2 Hz. All the images were processed by using Gwyddion Software v.2.65.

Quartz Crystal Microbalance (QCM). [6]-Gingerol LB films were studied using a Stanford Research Systems QCM.

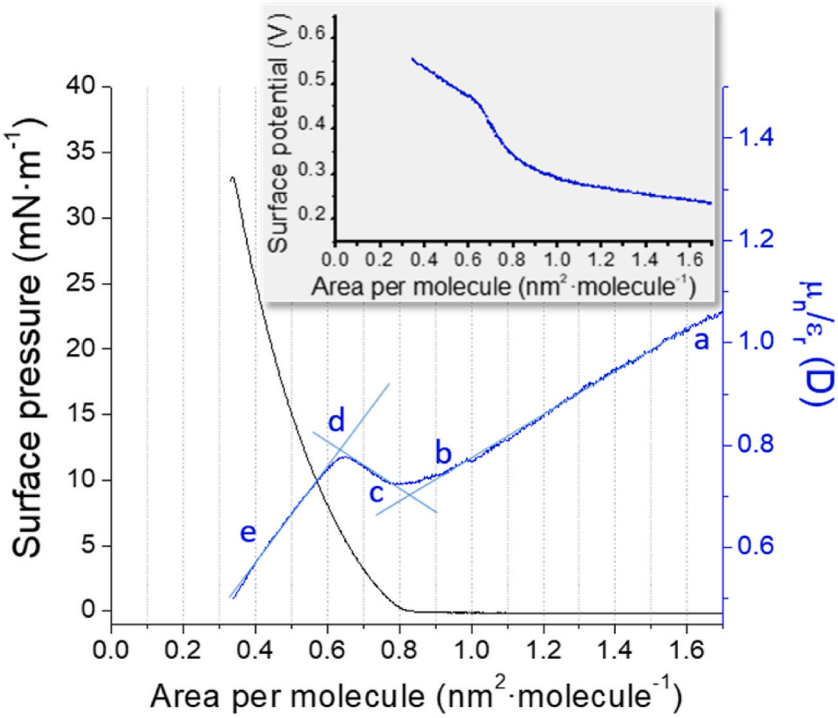

Fig. 3. Surface pressure and normalized surface potential isotherms of [6]-Gingerol. Inset: surface potential vs. area per molecule isotherm.

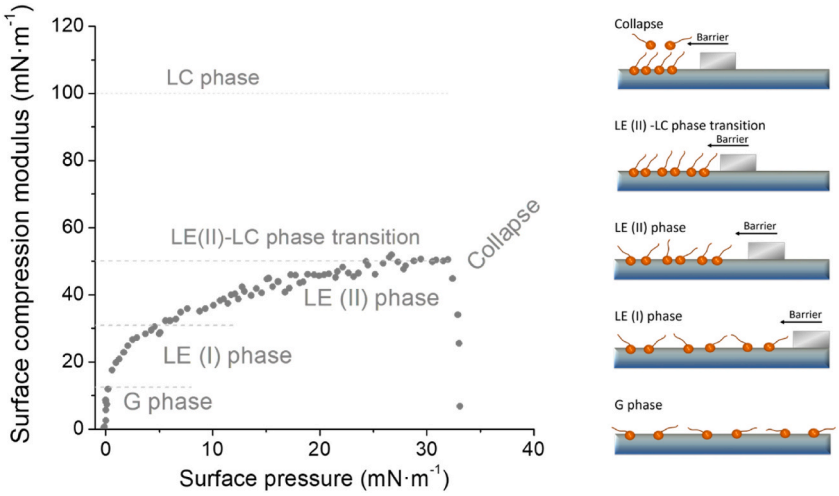

Fig. 4. Surface compression modulus vs. surface pressure for [6]-Gingerol, along with an illustrative model depicting the different phases and phase transitions observed in the surface pressure and surface potential isotherms.

3. Results and discussion

3.1. Surface behavior of [66]-Gingerol at the air-water interface

Langmuir films of [6]-Gingerol have been prepared at the air-water interface. A comprehensive study was conducted to determine the optimal conditions for preparing these films. [6]-Gingerol molecules tend to aggregate due to hydrogen bond formation, as evidenced by deviations from the Lambert-Beer law at concentrations as low as $5{\cdot}10^{-5}$ M (Fig. 2). The slope of the linear regression plot at low concentrations, where the Lambert-Beer law is followed, provides a molar absorptivity of approximately 3800 mol^{-1} L cm^{-1} for the maximum wavelength (282 nm). The maximum wavelength is consistent with previously published data, and the value of the molar absorptivity shows only minor differences possibly attributable to the different solvents used (chloroform in this paper and

methanol in the literature) [46].

Aggregation in the spreading solution should be avoided in Langmuir film preparation as it could lead to the formation of three-dimensional aggregates at the air-water interphase [43]. For this reason, diluted solutions of $1{\cdot}10^{-5}$ M of [6]-Gingerol in chloroform were spread at the air-water interface, so that the initial area per molecule was 2.15 nm^2 $molecule^{-1}$. Under these experimental conditions, reproducible isotherms of [6]-Gingerol were attained. The surface pressure vs. area per molecule isotherm of [6]-Gingerol is shown in Fig. 3 (depicted in black).

The take-off in the compression isotherm takes place at an area of ca. 0.8 nm^2. Further compression results in a monotonic increase in surface pressure as the area per molecule decreases, with the monolayer gradually transitioning to more ordered phases, culminating in a collapse at 33 mN m^{-1}. To extract further insights from the surface pressure vs. area per molecule isotherm, the surface compression modulus values, denoted here as K_s (inverse of the compressibility, C_s), were calculated using the equation [47]:

$$K_s = C_s^{-1} = -A\left(\frac{\partial \pi}{\partial A}\right)_T \tag{1}$$

The values of K_s obtained during the compression of the monolayer are presented in Fig. 4. The surface compression modulus provides information about the physical state of monolayers, closely tied to the packing and ordering of molecules at the air-water interface. Following the classification by Davies and Rideal [48], the different phases and phase transitions can be denoted as follows: values ranging from 12.5 to 50 mN m^{-1} signify a liquid expanded (LE) phase, values ranging from 100 to 250 mN m^{-1} denote a liquid condensed (LC) phase and values of K_s over 1000–2000 mN m^{-1} are indicative of a solid condensed (S) phase. An analysis of the (K_s - π) plot, indicates that the monolayer transition from the G into the LE phase occurs at a surface pressure of 0.2 mN m^{-1} and an area per molecule of 0.75 nm^2. Based on the K_s values and the surface potential vs. area per molecule isotherm (see Fig. 3 and the later discussion), we have identified a transition between two distinct liquid expanded states, LE(I)→LE(II), occurring at approximately 5 mN m^{-1}. At ca. 26 mN m^{-1}, a LE (II)→LC transition phase occurs, in line with Davies and Rideal's criteria, with $K_s > 50$ mN m^{-1}. The maximum value of K_s is 52 mN m^{-1}, reached at a surface pressure of 27 mN m^{-1}, representing the point at which the monolayer attains its highest stability. Subsequently, the monolayer collapses at a surface pressure of 33 mN m^{-1}, as evidenced by a drastic decrease in the surface compression modulus.

The reversibility of the monolayers as well as any eventual loss of material into the subphase were studied by successive hysteresis cycles in three compression-decompression cycles at a target surface pressure of 30 mN m^{-1} and returning surface pressure of 0 mN m^{-1}. A totally negligible hysteresis was observed for all the three cycles, which is indicative of no significant loss of [6]-Gingerol molecules in the subphase. The high reversibility of the [6]-Gingerol isotherm can be explained by the fluidity of the monolayer, which allows molecules to easily rearrange after each compression-decompression process.

The surface potential vs. area per molecule (ΔV-A) isotherm was also recorded to assess changes in the orientation of the molecules during the compression process and to gather additional insights into the phases and phase transitions of the monolayer. The inset of Fig. 3 shows the ΔV values obtained upon the compression process, with a gradual increase in ΔV values corresponding to the transition to more condensed phases as the monolayer is compressed [49]. The higher sensitivity of this technique results in phase and phase transitions that are discernible in the ΔV-A isotherms at larger areas compared to what is observed in the π-A isotherms. The surface potential of a monolayer is related to the dipole moment of the molecules within the monolayer according to the Helmholtz model [50]. The Helmholtz model conceptualizes the monolayer as a parallel plate condenser, comprising a sheet of uniformly distributed dipoles. In these circumstances, the surface potential can be expressed as:

$$\Delta V = \frac{\mu_n}{A \cdot \varepsilon_r \cdot \varepsilon_0} + \Psi_0 \tag{2}$$

where A represents the area per molecule, ε_r and ε_0 denote the relative dielectric constant and the permittivity of vacuum, respectively, μ_n represents the normal component of the dipole moment per molecule, and Ψ_0 is the double layer contribution in ionized monolayers, having a zero value in non-ionized monolayers as occurs in the [6]-Gingerol system. Demchak and Fort [51] proposed a three-layer capacitor model, wherein the monolayer surface potential for non-ionized monolayers is expressed as:

$$\Delta V = \frac{1}{A \cdot \varepsilon_0}\left(\frac{\mu_1}{\varepsilon_1} + \frac{\mu_2}{\varepsilon_2} + \frac{\mu_3}{\varepsilon_3}\right) \tag{3}$$

where μ_1/ε_1 corresponds to reorientation of water molecules; μ_2/ε_2 and μ_3/ε_3 are attributable to the reorganization of hydrophilic and hydrophobic group regions, respectively. Fig. 3 (right Y-axis) illustrates the μ_n/ε_r value for a [6]-Gingerol monolayer ($=\sum \mu_i/\ \varepsilon_i$). In Fig. 3, several distinct regions with a nearly linear μ_n/ε_r vs. A dependence are evident (highlighted by light blue lines), which is in good agreement with a non-ionizable monolayer. The μ_n/ε_r values in the a to b region are attributed here to the hydrophilic anchoring groups of the molecule as well as reorientation of the water molecules in the vicinity of the [6]-Gingerol molecules. This a to b region lies in the gas phase in the isotherm, exhibiting a consistently negative slope of μ_n/ε_r vs. A until ca. 0.85 nm^2 $molecule^{-1}$ (b point in Fig. 3), where the change in slope anticipates the take-off in the π-A isotherm. Subsequently, in the 0.85–0.77 nm^2 $molecule^{-1}$ region, the slope of μ_n/ε_r vs. A is close to zero (region b to c in Fig. 3), which is tentatively attributed here to a G→LE(I) transition, with the alkyl chain of [6]-Gingerol being progressively oriented towards a more vertical position. Further compression allows the monolayer to fully enter the LE(I) region within the 0.77–0.64 $nm^2{\cdot}molecule^{-1}$ region (c to d in Fig. 3), in which the molecules may adopt a more vertical orientation. Continued compression promotes lateral interactions between the alkyl chains of [6]-Gingerol, possibly with π-π interactions as well as hydrogen bonds between neighboring molecules [52], and the subsequent reorganization of water molecules

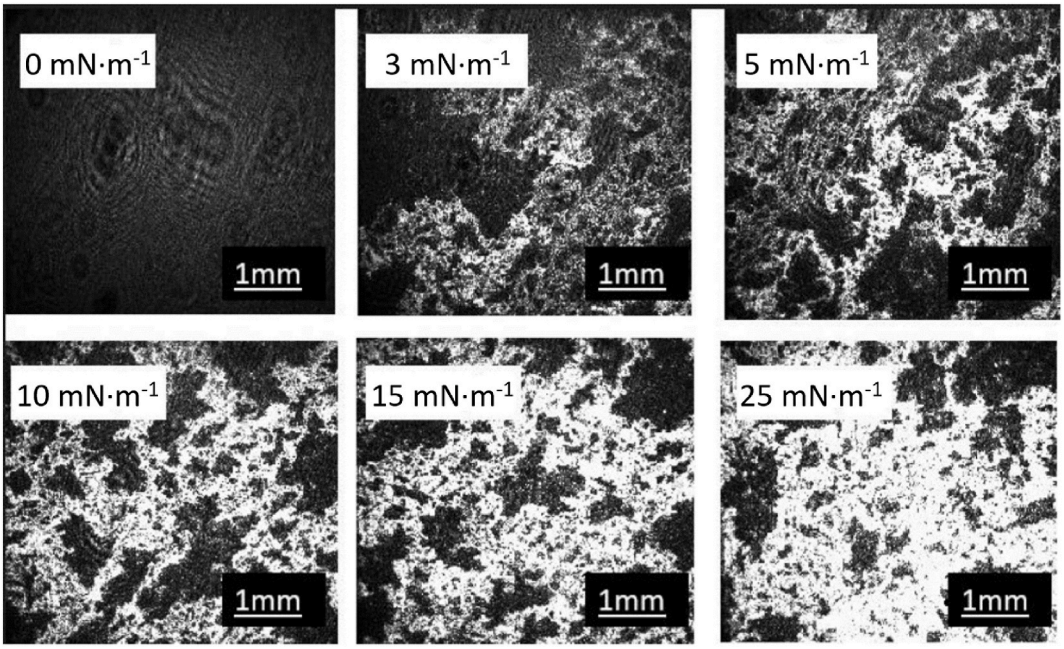

Fig. 5. BAM images for a [6]-Gingerol monolayer at the indicated surface pressures.

resulting in another region with a negative slope, which we attribute to a LE(II) phase (*d* to *e* in Fig. 3). The μ_n/ε_r value before the collapse of the monolayer is approximately 0.55 D, which provides a measurement of the polarity of the [6]-Gingerol monolayer at the air-water interface in its most ordered state prior to the formation of a disordered multilayer. This value reflects the additive contribution of the dipole moment of [6]-Gingerol and the contribution of the presence of ordered water molecules at the air-water interface [53]. The cartoon in Fig. 4 provides an illustrative model of the different phases and phase transitions for [6]-Gingerol based on the surface pressure, surface compression modulus, and surface potential isotherms.

The *in situ* formation of the monolayer was visualized with a Brewster Angle Microscope (BAM). Fig. 5 shows representative images recorded at the indicated surface pressures. At the beginning of the compression process, the presence of [6]-Gingerol cannot be detected in the BAM image, which is indicative of a gas phase [54]. However, as the surface pressure increases, domains become clearly visible. This formation of domains is interpreted here in terms of the large tendency of this compound to aggregate, mainly due to the formation of intermolecular hydrogen bonds. These domains soon cover most of the image indicating an increase in the surface density of the film layer. Importantly, the brightness of the images increases as the surface pressure rises, which is indicative of a gradual tilting of the molecules within the monolayer and consequent thickening [45].

The surface behavior of [6]-Gingerol, as analyzed above, is tentatively interpreted here in terms of its chemical structure: the presence of two hydrogen bond donor atoms and four hydrogen bond accepting atoms allow the formation of intermolecular interactions, not only between [6]-Gingerol molecules but also between [6]-Gingerol and the water molecules in the subphase. Additionally, the high number of bonds capable of rotation translates into high conformational flexibility, which may explain the liquid expanded behavior despite high surface pressures being reached. Moreover, the presence of a π-phenolic ring could result in a π-π intermolecular stacking.

3.2. Supported monolayers of [6]-Gingerol

The deposition of the [6]-Gingerol Langmuir films onto solid supports at a surface pressure of 27 mN m^{-1} was quantified using a Quartz Crystal Microbalance (QCM) [55,56]. This surface pressure was chosen as it corresponds to the point at which the *Ks* value reaches its maximum. The frequency change of the QCM crystal, Δf in Hz, was determined, and the Sauerbrey equation [57] was applied:

$$\Delta f = -C_f \cdot \varphi \quad (4)$$

where φ is the change in mass per unit area in g·cm^{-2}, and C_f is the sensitivity factor for the crystal (56.6 Hz μg^{-1} cm^2 for our 5 MHz crystal at room temperature). The surface coverage of the transferred films, Γ, at a surface pressure of 27 mN m^{-1} was 7.5×10^{-10} mol cm^{-2}. This value is higher than the surface density for the Langmuir film at 27 mN m^{-1}, namely, 4.3×10^{-10} mol cm^{-2}. This result is indicative of a reorganization of the [6]-Gingerol molecules upon the transference onto a gold substrate.

To further characterize the LB monolayers, atomic force microscopy (AFM) images of [6]-Gingerol transferred onto freshly cleaved mica were obtained. The deposition of the film onto the substrates was performed by using the vertical dipping method. Transferences

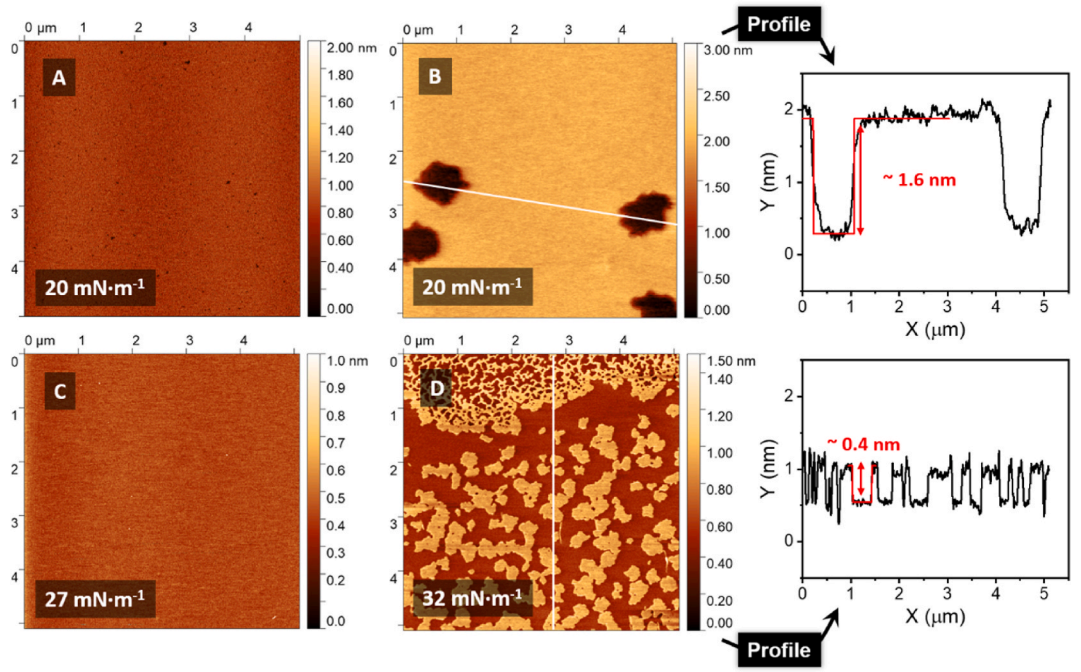

Fig. 6. AFM images for [6]-Gingerol monolayers together with the indicated profiles (white lines in the AFM images). (A) 5 × 5 μm^2 image for an LB film transferred at 20 mN m^{-1}. (B) 5 × 5 μm^2 image for an LB film transferred at 20 mN m^{-1}, intentionally showing a region where some uncovered areas are visible. (C) 5 × 5 μm^2 image for an LB film transferred at 27 mN m^{-1} and (D) 5 × 5 μm^2 image for an LB film transferred at 32 mN m^{-1}. Right: cross-section profiles for the indicated images.

at several target surface pressures were carried out, namely 20, 27, and 32 mN m^{-1} (Fig. 6). Films transferred at 20 mN m^{-1} are quite homogeneous, though some small holes are present (Fig. 6A). These holes are too narrow to accurately determine the monolayer height, so we scanned multiple areas in search of defects. In one region (Fig. 6B), we found relatively large uncovered areas surrounded by a homogeneous film. The film thickness, calculated from a statistical analysis of cross-section profiles at the boundary between these uncovered regions and the film, is 1.61 ± 0.08 nm. This, along with the molecular length of [6]-Gingerol in its fully extended configuration (1.8 nm, Fig. 1), indicates that the molecules are oriented at an average tilt angle of about 62° relative to the substrate surface. Very homogeneous films with no apparent holes are obtained at a surface pressure of transference of 27 mN m^{-1} (Fig. 6C). This surface pressure corresponds to the maximum K_s value obtained and the highest monolayer stability, with an RMS roughness of 0.05 ± 0.01 nm. Transferences at 32 mN m^{-1} result in the presence of higher structures, with a height of 0.42 ± 0.03 nm (Fig. 6D). This is tentatively interpreted here as the expulsion of some molecules from the monolayer, with these molecules lying on the second layer in a relatively flat orientation according to the height of the observed domains. The formation of bilayers, in which the upper layer exhibits a lying-down configuration of the molecules, has been previously observed in certain model cell membranes [58]. Eventually, this expulsion of the molecules from the monolayer results in the collapse of the monolayer, which is in good agreement with the surface pressure vs. area per molecule isotherm and the drastic drop in the *Ks* values observed at 33 mN m^{-1}.

4. Conclusions

In this contribution, we investigated the surface behavior of [6]-Gingerol at the air-water interface at a temperature of 21 °C. Our findings reveal reproducible surface pressure vs. area per molecule isotherms with negligible hysteresis. Through a comprehensive analysis of π-*A* and ΔV-*A* isotherms, together with the determination of the surface compression modulus, we observed a sequence of phases in the monolayer: gas phase, followed by liquid expanded (I) and liquid expanded (II) phase, and an incipient transition to a liquid condensed phase, with the maximum stability achieved at a surface pressure of 27 mN m^{-1}. The monolayer collapses at 33 mN m^{-1}. Brewster Angle Microscopy images further confirm the surface behavior of [6]-Gingerol at the air-water interface. These images exhibit increasing brightness as the monolayer is compressed, indicating an increase in thickness and a transition in molecular orientation from lying down to a more upright position. [6]-Gingerol monolayers were successfully transferred onto solid supports forming homogeneous films at a target surface pressure of transference of 27 mN m^{-1}, with a surface density of 7.5 × 10^{-10} mol cm^{-2} in QCM substrates.

These results are crucial from a fundamental perspective, as they provide support for future investigations on the interaction of [6]-Gingerol with model cell membranes. Such studies aim to enhance our understanding of the mechanism of action of this xenobiotic and explore how [6]-Gingerol could be combined with membrane components to achieve an optimal composition for the preparation of drug delivery vesicles. In this context, [6]-Gingerol could serve as a co-adjuvant incorporated into the external membrane of the

vesicle. Ongoing research in our lab is dedicated to further exploring these prospects.

CRediT authorship contribution statement

Lara Adwan: Writing – review & editing, Writing – original draft, Methodology, Investigation. **Laura Dotor:** Writing – review & editing, Supervision, Investigation. **María Graciela Pino:** Writing – review & editing, Methodology, Investigation. **Adriana Gil:** Investigation. **Santiago Martin:** Writing – review & editing, Supervision. **Pilar Cea:** Writing – review & editing, Writing – original draft, Validation, Supervision, Funding acquisition, Formal analysis, Conceptualization.

Declaration of competing interest

The authors declare that they have no known competing financial interests or personal relationships that could have appeared to influence the work reported in this paper.

Acknowledgements

Authors are grateful to DGA/Fondos FEDER (Construyendo Europa desde Aragón) for funding the research group Platón (E31_23R). M.G.P. acknowledges the grant provided by the Universidad de Panama for the realization of her PhD at Universidad de Zaragoza. Authors also acknowledge the use of Servicio General de Apoyo a la Investigación (SAI) as well as the Laboratory for Advanced Microscopies (LMA) from University of Zaragoza.

References

[1] L.M. Mayr, D. Bojanic, Novel trends in high-throughput screening, COPHAR 9 (5) (2009) 580–588.
[2] A.M. Bode, D. Zigang, The amazing and mighty ginger, in: Herbal Medicine: Biomolecular and Clinical Aspects, second ed., 2011.
[3] H.-C. Lien, W.M. Sun, Y.-H. Chen, H. Kim, W. Hasler, C. Owyang, Effects of ginger on motion sickness and gastric slow-wave dysrhythmias induced by circular vection, Am. J. Physiol. Gstrointest. Liver Physiol. 284 (3) (2003) G481–G489.
[4] A. AlAskar, N.A. Shaheen, A.H. Khan, N. AlGhasham, M.A. Mendoza, D.B. Matar, G. Gmati, M. AlJeraisy, A. AlSuhaibani, Effect of daily ginger consumption on platelet aggregation, J. Herb. Med. 20 (2020) 100316.
[5] N.M. Roudsari, N.-A. Lashgari, S. Momtaz, B. Roufogalis, A.H. Abdolghaffari, A. Sahebkar, Ginger: a complementary approach for management of cardiovascular diseases, Biofactors 47 (6) (2021) 933–951.
[6] Y. Liu, S. Deng, Z. Zhang, Y. Gu, S. Xia, X. Bao, X. Cao, Y. Xu, 6-Gingerol attenuates microglia-mediated neuroinflammation and ischemic brain injuries through Akt-mTOR-STAT3 signaling pathway, Eur. J. Pharmacol. 883 (2020) 173294.
[7] A. Alipour, V. Baradaran Rahimi, V.R. Askari, Promising influences of gingerols against metabolic syndrome: a mechanistic review, Biofactors 48 (5) (2022) 993–1004.
[8] C.T. Oliveira, D.R. Lacerda, M.C. Zicker, L.B. Martins, M.M. Teixeira, R.L.B. de Araujo, A.V.M. Ferreira, Ginger (zingiber officinale rosc.) ameliorated metabolic and inflammatory dysfunction induced by high-refined carbohydrate-containing diet in mice, J. Med. Food 22 (1) (2018) 38–45.
[9] F. Shidfar, A. Rajab, T. Rahideh, N. Khandouzi, S. Hosseini, S. Shidfar, The effect of ginger (Zingiber officinale) on glycemic markers in patients with type 2 diabetes, JCIM 12 (2) (2015) 165–170.
[10] P. Azimi, R. Ghiasvand, A. Feizi, J. Hosseinzadeh, M. Bahreynian, M. Hariri, H. Khosravi-Boroujeni, Effect of cinnamon, cardamom, saffron and ginger consumption on blood pressure and a marker of endothelial function in patients with type 2 diabetes mellitus: a randomized controlled clinical trial, Blood Pres. 25 (3) (2016) 133–140.
[11] M.T. Sohail, M.I. Chaudhry, M.K. Usman, T. Mian, M.N. Ishaq, Efficacy and tolerance of atrisin in degenerative and inflammatory joint disorders, Phytother Res. 19 (4) (2005) 365–368.
[12] E. Ernst, M.H. Pittler, Efficacy of ginger for nausea and vomiting: a systematic review of randomized clinical trials, Br. J. Anaesth. 84 (3) (2000) 367–371.
[13] M. Okamoto, H. Irii, Y. Tahara, H. Ishii, A. Hirao, H. Udagawa, M. Hiramoto, K. Yasuda, A. Takanishi, S. Shibata, I. Shimizu, Synthesis of a new [6]-Gingerol analogue and its protective effect with respect to the development of metabolic syndrome in mice fed a high-fat diet, J. Med. Chem. 54 (18) (2011) 6295–6304.
[14] Q.-Q. Mao, X.-Y. Xu, S.-Y. Cao, R.-Y. Gan, H. Corke, T. Beta, H.-B. Li, Bioactive compounds and bioactivities of ginger (zingiber officinale Roscoe), Foods 8 (6) (2019) 185.
[15] Y.Y. Wong, Y.-L. Chow, Exploring the potential of spice-derived phytochemicals as alternative antimicrobial agents, eFood 5 (1) (2024) e126.
[16] J.W. Choi, H.-Y. Park, M.S. Oh, H.H. Yoo, S.-H. Lee, S.K. Ha, Neuroprotective effect of 6-paradol enriched ginger extract by fermentation using Schizosaccharomyces pombe, J. Funct.Foods 31 (2017) 304–310.
[17] J.G. Choi, S.Y. Kim, M. Jeong, M.S. Oh, Pharmacotherapeutic potential of ginger and its compounds in age-related neurological disorders, Clin. Pharm. Therap. 182 (2018) 56–69.
[18] Y. Jiang, D.K. Turgeon, B.D. Wright, E. Sidahmed, M.T. Ruffin, D.E. Brenner, A. Sen, S.M. Zick, Effect of ginger root on cyclooxygenase-1 and 15-hydroxy-prostaglandin dehydrogenase expression in colonic mucosa of humans at normal and increased risk for colorectal cancer, Eur. J. Cancer Prev. 22 (5) (2013).
[19] S.M. Nachvak, D. Soleimani, M. Rahimi, A. Azizi, M. Moradinazar, M.H. Rouhani, B. Halashi, A. Abbasi, M. Miryan, Ginger as an anticolorectal cancer spice: a systematic review of in vitro to clinical evidence, Food Sci. Nutr. 11 (2) (2023) 651–660.
[20] T. Dorai, B.B. Aggarwal, Role of chemopreventive agents in cancer therapy, Cancer Lett. 215 (2) (2004) 129–140.
[21] H. Sung, J. Ferlay, R.L. Siegel, M. Laversanne, I. Soerjomataram, A. Jemal, F. Bray, Global cancer statistics 2020: GLOBOCAN estimates of incidence and mortality worldwide for 36 cancers in 185 countries, CA A Cancer J. Clin. 71 (3) (2021) 209–249.
[22] S. Sang, H.D. Snook, F.S. Tareq, Y. Fasina, Precision research on ginger: the type of ginger matters, J. Agric. Food Chem. 68 (32) (2020) 8517–8523.
[23] M.F. Mahomoodally, M.Z. Aumeeruddy, K.R.R. Rengasamy, S. Roshan, S. Hammad, J. Pandohee, X. Hu, G. Zengin, Ginger and its active compounds in cancer therapy: from folk uses to nano-therapeutic applications, Semin. Cancer Biol. 69 (2021) 140–149.
[24] S. Dugasani, M.R. Pichika, V.D. Nadarajah, M.K. Balijepalli, S. Tandra, J.N. Korlakunta, Comparative antioxidant and anti-inflammatory effects of [6]-gingerol, [8]-gingerol, [10]-gingerol and [6]-shogaol, J. Ethnopharmacol. 127 (2) (2010) 515–520.
[25] S. Wang, C. Zhang, G. Yang, Y. Yang, Biological properties of 6-gingerol: a brief review, Nat. Prod. Commun. 9 (7) (2014), 1934578X1400900736.
[26] H.-S. Kim, S.-H. Lee, Y. Byun, H.-D. Park, 6-Gingerol reduces Pseudomonas aeruginosa biofilm formation and virulence via quorum sensing inhibition, Sci. Rep. 5 (1) (2015) 8656.
[27] R.M.T. de Lima, A.C. dos Reis, A.-A.P.M. de Menezes, J.V.d.O. Santos, J.W.G.d.O. Filho, J.R.d.O. Ferreira, M.V.O.B. de Alencar, A.M.O.F. da Mata, I.N. Khan, A. Islam, S.J. Uddin, E.S. Ali, M.T. Islam, S. Tripathi, S.K. Mishra, M.S. Mubarak, A.A.d.C. Melo-Cavalcante, Protective and therapeutic potential of ginger (Zingiber officinale) extract and [6]-gingerol in cancer: a comprehensive review, Phytother Res. 32 (10) (2018) 1885–1907.

[28] J. McHugh, Getting to the root of the anti-inflammatory effects of ginger, Nat. Rev. Rheumatol. 17 (3) (2021) 130, 130.
[29] S.-q. Ma, Z. Guo, F.-y. Liu, S.-G. Hasan, D. Yang, N. Tang, P. An, M.-y. Wang, H.-m. Wu, Z. Yang, D. Fan, Q.-z. Tang, 6-Gingerol protects against cardiac remodeling by inhibiting the p38 mitogen-activated protein kinase pathway, Acta Pharmacol. Sin. 42 (10) (2021) 1575–1586.
[30] K. Vimala, S. Kannan, Chapter Ten - phyto-drug conjugated nanomaterials enhance apoptotic activity in cancer, in: R. Donev (Ed.), Advances in Protein Chemistry and Structural Biology, Academic Press, 2021, pp. 275–305.
[31] N. Promdam, P. Panichayupakaranant, [6]-Gingerol: a narrative review of its beneficial effect on human health, Food Chemistry Advances. 1 (2022) 100043.
[32] S.-z. Jiang, N.-s. Wang, S.-q. Mi, Plasma pharmacokinetics and tissue distribution of [6]-gingerol in rats, Biopharm Drug Dispos. 29 (9) (2008) 529–537.
[33] Y. Xu, Q. Wang, Y. Feng, C.K. Firempong, Y. Zhu, E. Omari-Siaw, Y. Zheng, Z. Pu, X. Xu, J. Yu, Enhanced oral bioavailability of [6]-Gingerol-SMEDDS: preparation, in vitro and in vivo evaluation, J. Funct.Foods 27 (2016) 703–710.
[34] F. Man, C. Meng, Y. Liu, Y. Wang, Y. Zhou, J. Ma, R. Lu, The study of ginger-derived extracellular vesicles as a natural nanoscale drug carrier and their intestinal absorption in rats, AAPS PharmSciTech 22 (6) (2021) 206.
[35] P. Thangavelu, V. Sundaram, K. Gunasekaran, B. Mujyambere, S. Raju, A. Kannan, A. Arasu, K. Krishna, J. Ramamoorthi, S. Ramasamy, T. Velusamy, S. Samiappan, Development of optimized novel liposome loaded with 6-gingerol and assessment of its therapeutic activity against NSCLC in vitro and in vivo experimental models, Chem. Phys. Lipids 245 (2022) 105206.
[36] X. Chen, Y. Zhou, J. Yu, Exosome-like nanoparticles from ginger rhizomes inhibited NLRP3 inflammasome activation, Mol. Pharmaceutics. 16 (6) (2019) 2690–2699.
[37] O.N. Oliveira, L. Caseli, K. Ariga, The past and the future of Langmuir and Langmuir–blodgett films, Chem. Rev. 122 (6) (2022) 6459–6513.
[38] M. Jurak, K. Szafran, P. Cea, S. Martín, Analysis of molecular interactions between components in phospholipid-immunosuppressant-antioxidant mixed Langmuir films, Langmuir 37 (18) (2021) 5601–5616.
[39] L. Dotor, J.M. García-Pinilla, S. Martín, P. Cea, Langmuir and Langmuir-Blodgett technologies as nanoarchitectonic tools for the incorporation of curcumin in membrane systems, Nanoscale 15 (6) (2023) 2891–2903.
[40] P. Cea, C. Lafuente, J.S. Urieta, M.C. Lopez, F.M. Royo, Langmuir and Langmuir-Blodgett films of a viologen derivative, Langmuir 14 (25) (1998) 7306–7312.
[41] S.A. Hussain, P.K. Paul, D. Bhattacharjee, Role of various LB parameters on the optical characteristics of mixed Langmuir–Blodgett films, J. Phys. Chem. Solids. 67 (12) (2006) 2542–2549.
[42] P.K. Paul, S.A. Hussain, D. Bhattacharjee, Photophysical characterizations of 2-(4-biphenylyl)-5 phenyl-1,3,4-oxadiazole in restricted geometry, J. Lumin. 128 (1) (2008) 41–50.
[43] A. Villares, G. Pera, S. Martín, R.J. Nichols, D.P. Lydon, L. Applegarth, A. Beeby, P.J. Low, P. Cea, Fabrication, characterization, and electrical properties of Langmuir−Blodgett films of an acid terminated Phenylene−Ethynylene oligomer, Chem. Mater. 22 (6) (2010) 2041–2049.
[44] A. Villares, D.P. Lydon, L. Porrès, A. Beeby, P.J. Low, P. Cea, F.M. Royo, Preparation of ordered films containing a phenylene ethynylene oligomer by the Langmuir-Blodgett technique, J. Phys. Chem. B 111 (2007) 7201–7209.
[45] G. Pera, A. Villares, M.C. Lopez, P. Cea, D.P. Lydon, P.J. Low, Preparation and characterization of Langmuir and Langmuir-Blodgett films from a nitrile-terminated tolan, Chem. Mater. 19 (4) (2007) 857–864.
[46] S. Zick, M. Ruffin, Z. Djuric, D. Normolle, D. Brenner, Quantitation of 6-, 8- and 10-gingerols and 6-shogaol in human plasma by high-performance liquid chromatography with electrochemical detection, Int. J. Biomed. Sci. 6 (3) (2010) 233–240.
[47] G.L. Gaines, Insoluble Monolayers at Liquid-Gas Interface, Interscience. John Wiley & Sons., New York, 1966.
[48] J.T. Davies, E.K. Rideal, Interfacial Phenomena, Academic Press, New York, 1961.
[49] V. Vogel, D. Möbius, Local surface potentials and electric dipole moments of lipid monolayers: contributions of the water/lipid and the lipid/air interfaces, J. Colloid Interface Sci. 126 (2) (1988) 408–420.
[50] H. Helmholtz, Abhandlungen Thermod, 1902, p. 51.
[51] R.J. Demchak, J. Fort, J. Colloid Interface Sci. 46 (1974) 191.
[52] A. Villares, D.P. Lydon, L. Porres, A. Beeby, P.J. Low, P. Cea, F.M. Royo, Preparation of ordered films containing a phenylene ethynylene oligomer by the Langmuir-Blodgett technique, J. Phys. Chem. B 111 (25) (2007) 7201–7209.
[53] V. Tsukanova, C. Salesse, On the nature of conformational transition in poly(ethylene glycol) chains grafted onto phospholipid monolayers, J. Phys. Chem. B 108 (2004) 10754–10764.
[54] X. Xu, Y. Shao, W. Wang, J. Liao, H. Liu, W. Zhang, W.-B. Zhang, S. Yang, Phase behaviors of giant surfactants with different numbers of fluorinated polyhedral oligomeric silsesquioxane “heads” and one poly(ethylene oxide) “tail” at the air–water interface, Langmuir 37 (37) (2021) 11084–11092.
[55] P. Cea, S. Martín, A. González-Orive, H.M. Osorio, P. Quintín, L. Herrer, Nanofabrication and electrochemical characterization of self-assembled monolayers sandwiched between metal nanoparticles and electrode surfaces, J. Chem. Edu. 93 (8) (2016) 1441–1445.
[56] J. Wei, Y. Shao, S. Qiao, A. Li, S. Hou, W.-B. Zhang, Biomacromolecular characterizations using state-of-the-art quartz crystal microbalance with dissipation, Anal. Chem. 95 (45) (2023) 16435–16446.
[57] G. Sauerbrey, The use of quartz oscillators for weighing thin layers and for microweighing, Z. Physik. 155 (2) (1959) 206–222.
[58] S. Ruiz-Rincon, A. Gonzalez-Orive, J.M. de la Fuente, P. Cea, Reversible monolayer-bilayer transition in supported phospholipid LB films under the presence of water: morphological and nanomechanical behavior, Langmuir 33 (30) (2017) 7538–7547.